

Micromagnetic Simulations of Antiskyrmions

Ross Knapman

Level 4 Project, MPhys Physics

Supervisor: Prof P. Hatton

Department of Physics, Durham University

Submitted: April 23, 2019

Magnetic skyrmions are topologically-protected vortex-like solitons that separate regions of reversed magnetic moments from those surrounding them. Owing to their small size in comparison with other magnetic structures, interest in such structures has increased rapidly in recent years, with suggested applications in ultra-dense information storage and processing. Bloch and Néel skyrmions exhibit homochiral structures, whilst antiskyrmions exhibit multichirality and possess an opposite topological charge. Despite the resonance dynamics of Bloch and Néel skyrmions being well-understood, knowledge of the eigenmodes of antiskyrmions is currently lacking. In this work, we use micromagnetic simulations to demonstrate the rich dynamics of antiskyrmions at resonance. Additionally, we study the dynamics of antiskyrmions in a one-dimensional lattice, which has implications for their use in racetrack memory devices.

Contents

1. Introduction to Skyrmions	3
1.1. Developments in Skyrミonics	3
1.2. Skyrmion Spin Textures	4
1.3. (Anti-)skyrmion Dynamics and Applications	6
2. Micromagnetics	7
3. Magnetic Interactions	8
3.1. Symmetric Exchange Energy	8
3.2. Dzyaloshinskii-Moriya Energy	9
3.3. Uniaxial Anisotropy Energy	10
3.4. Zeeman Interaction Energy	11
3.5. Demagnetisation Energy	11

4. Resonance Calculations	12
4.1. Ringdown Method	12
4.2. Fourier Analysis	13
4.3. Eigenvalue Method	13
5. Resonances of an Antiskyrmion in a Nanodisk	14
5.1. Introduction	14
5.2. Comparison of Finite-Difference and Finite-Element Simulations	15
5.3. Comparison of the Ringdown and Eigenvalue Methods	16
5.4. Behaviour of the Modes	17
5.5. Effect of Saturation Magnetisation on Resonance Modes	19
6. Resonances of Antiskyrmions in a Lattice	21
6.1. Introduction	21
6.2. Square Lattice Resonance Modes	23
6.3. Hexagonal Lattice Resonance Modes	24
7. Dynamics of Antiskyrmions in Nanotracks	26
7.1. Introduction	26
7.2. Antiskyrmion-Antiskyrmion Interactions	26
7.3. Oscillations of Antiskyrmions in a Nanotrack	27
8. Conclusions and Further Work	28
8.1. Conclusions	28
8.2. Potential Future Investigations	29
Acknowledgments	29
References	29
A. Effect of Sample Thickness on the Power Spectra	31
B. Effect of Externally-Applied Field on the Power Spectra	32

1. INTRODUCTION TO SKYRMIONS

1.1. Developments in Skyrmionics

The skyrmion was originally proposed in the mid-20th century by T. Skyrme as a model for nucleons in which particles are viewed as topologically-protected field configurations,^{1–5} characterised by a topological integer which cannot be changed by a continuous deformation. In the time since, skyrmions have been seen to be relevant in systems such as Bose-Einstein condensates,⁶ superconductors,⁷ liquid crystals,⁸ and, as discussed in this work, chiral magnets.

Magnetic skyrmions (referred to henceforth as simply “skyrmions”) have seen a significant increase in interest in recent years. They were first predicted by A. N. Bogdanov and D. A. Yablonskii in 1989,⁹ who referred to them as vortices. Bogdanov subsequently published various papers investigating such magnetic “vortices”,^{10–13} before relating them to Skyrme’s model in 2006.¹⁴ In 2009, Mühlbauer et. al. observed skyrmions in a magnetic system for the first time¹⁵ using small-angle neutron scattering of MnSi, associating the six-fold diffraction pattern that appears in the plane perpendicular to the external field, and is independent of the crystal’s orientation, resulting from such spin textures with the previously-unexplained A-phase. Skyrmions were first observed in real space in 2010 using Lorentz transmission electron microscopy.¹⁶

Skyrmions can be stabilised in chiral magnets by a variety of mechanisms, namely through long-range dipolar interactions,¹⁷ frustrated exchange interactions,¹⁸ four-spin exchange interactions,¹⁹ and the Dzyaloshinskii-Moriya interaction (DMI), which is the method of stabilisation of skyrmions that we focus on in this work. It is a type of exchange interaction that results from the breaking of inversion symmetry in the system, whose form depends on the specific geometry of the symmetry breaking. This is discussed in more detail in Section 3.2. As can be seen in the phase diagram in Fig. 1, the skyrmion spin texture is the ground

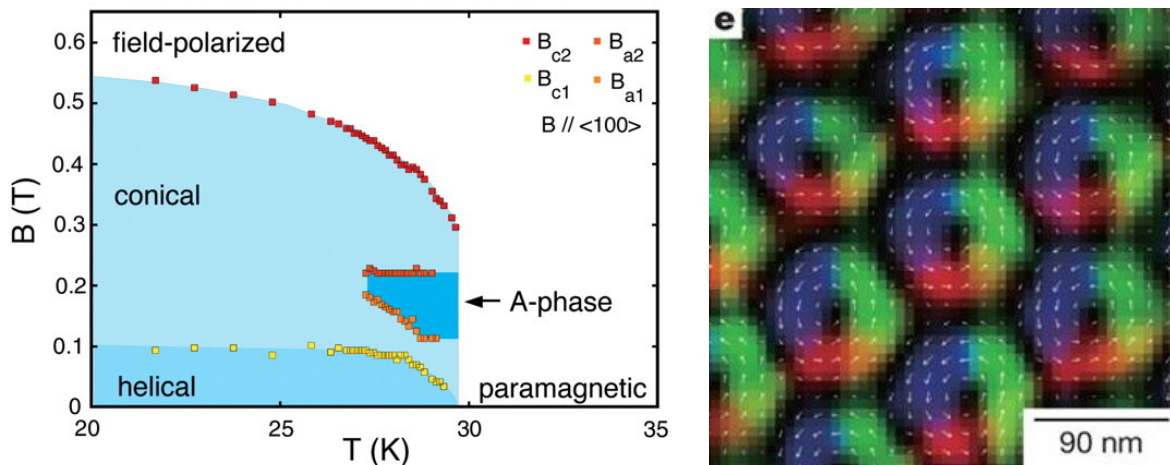


FIG. 1: Left: Experimentally-observed magnetic phase diagram of MnSi.¹⁵ Right: Skyrmions observed in real-space using LTEM.¹⁶

state of the system for a small subset of conditions, known as the “skyrmion pocket” (labelled the “A-phase” in the diagram). This occurs when the competition between the interactions described in Section 3 favours the formation of skyrmions. By the nature of the micromagnetic models used in this work, we consider states at a temperature of $T = 0$ K, where skyrmion states are metastable (but not ground) states.

1.2. Skyrmion Spin Textures

To define magnetic skyrmions, we consider the mapping which assigns to each point on a 2-sphere another point on a 2-sphere, $\mathbb{S}^2 \rightarrow \mathbb{S}^2$.²⁰ Graphically, this can be illustrated by covering a sphere in (2+1)-dimensional space with a continuous vector field. In the top row of Fig. 2, this is shown for discrete samples of the continuous vector field. In order to obtain the required spin texture in a two-dimensional plane, we consider a mapping $\mathbb{S}^2 \rightarrow \mathbb{R}^2$, known as a stereographic projection. This can be considered graphically by placing the aforementioned “studded sphere” tangent to the Euclidean plane at its south pole, and projecting the vector “studs” onto the plane along the line connecting the sphere’s north pole and the plane. This results in a one-to-one mapping between the 2-sphere and the plane, defined at every point on the sphere except the north pole, which corresponds to the limit $r \rightarrow \infty$, where r is the in-plane distance from the point where the south pole of the sphere touches the plane. The results of such a projection are shown in the middle row of Fig. 2.

Whilst there is some debate as to how a skyrmion is defined (due to the existence of topologically-identical magnetic bubbles),^{21–23} a useful quantity characterising the object’s nature is the topological charge, or \mathbb{S}^2 winding number (i.e. the number of times the vector sum of the normalised magnetisation vectors wraps a unit sphere), N_{sk} , given by

$$N_{\text{sk}} = -\frac{1}{4\pi} \int_{\mathbb{R}^2} d^2r \mathbf{m} \cdot (\partial_x \mathbf{m} \times \partial_y \mathbf{m}), \quad (1)$$

where $\mathbf{m}(\mathbf{r})$ is the unit vector of the magnetisation at position \mathbf{r} , such that the local magnetisation is given by $\mathbf{M}(\mathbf{r}) = M_s \mathbf{m}$, where M_s is the saturation magnetisation. The preceding minus sign ensures that $N_{\text{sk}} = 1$ for skyrmions and $N_{\text{sk}} = -1$ for antiskyrmions. This quantity has the property that it cannot be changed by a continuous deformation of the magnetisation vectors.

We can parameterise the skyrmion spin texture as

$$\mathbf{m}(\mathbf{r}) = [\cos \Phi(\mathbf{r}) \sin \Theta(\mathbf{r}), \sin \Phi(\mathbf{r}) \sin \Theta(\mathbf{r}), \cos \Theta(\mathbf{r})], \quad (2)$$

where

$$\Phi(\mathbf{r}) = m\phi + \eta, \quad (3)$$

$$\Theta(\mathbf{r}) = \Theta(r), \quad (4)$$

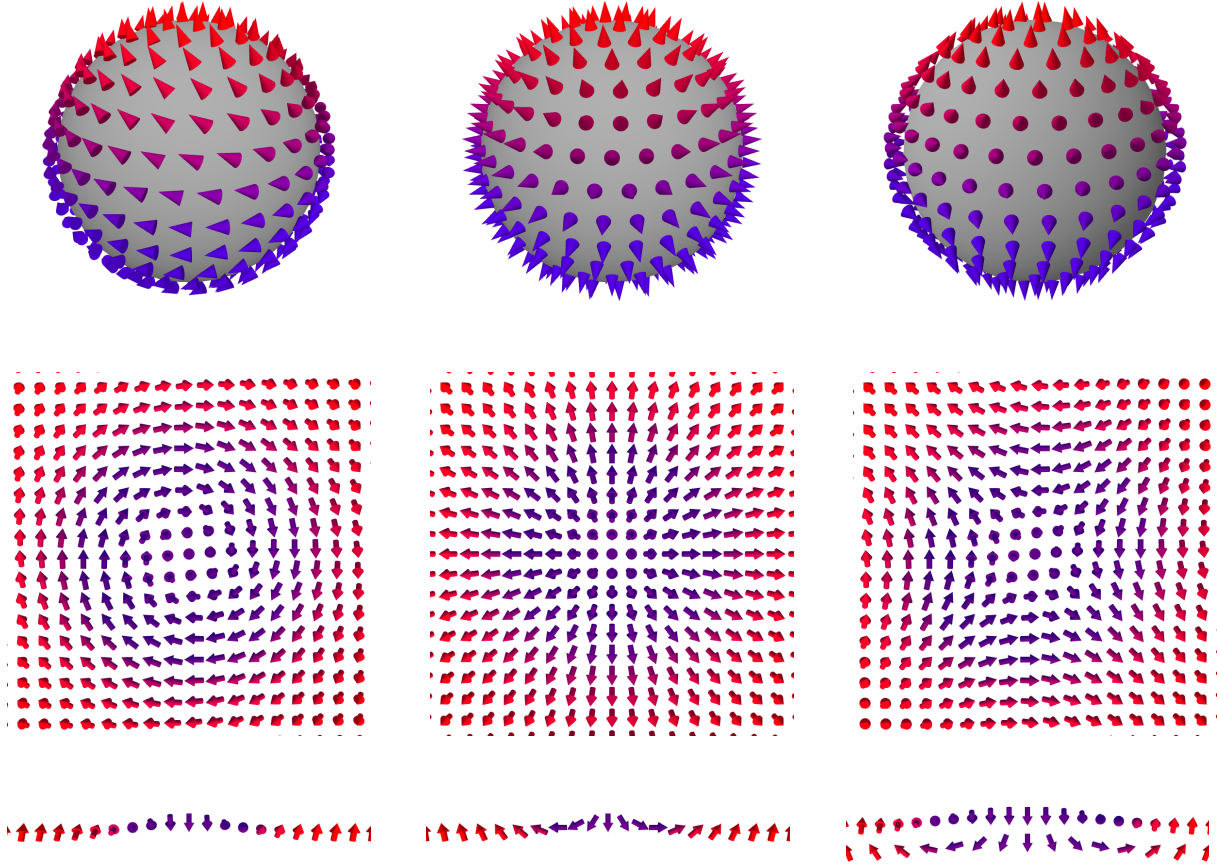


FIG. 2: Top row: “Studded spheres” used to construct the skyrmion spin textures via a stereographic projection. Middle row (from left to right): Bloch-, Néel-, and antiskyrmion spin textures resulting from the stereographic projections of the corresponding spheres in the top row. Bottom row: Radial profiles of the various types of skyrmion spin structures. For the antiskyrmion, the $y = 0$ and $y = x$ cases are shown, where \hat{x} runs towards the right-hand side of the page and \hat{y} runs up the page.

and

$$\mathbf{r} = (r \cos \phi, r \sin \phi). \quad (5)$$

Where r is as previously described and ϕ is the angle in the $x - y$ plane. \mathbf{m} points along the $+\hat{z}$ direction as $r \rightarrow \infty$ and along the $-\hat{z}$ direction at $r = 0$. The quantity $m \in \mathbb{R}$ is known as the vorticity and determines N_{sk} , while the helicity, $\eta \in \mathbb{R}$ does not. The magnetisation profile of the skyrmion depends on the type of DMI, which is in turn determined by the symmetry class of the material. Materials with the T or O symmetry classes exhibit a DMI that can stabilise Bloch skyrmions, which have $m = 1$ and $\eta = (n + 1/2)\pi$, $n \in \mathbb{Z}$. Materials with interfacial DMI or crystals with the C_{nv} , $n > 2$ symmetry class can stabilise Néel skyrmions, which have $m = 1$ and $\eta = n\pi$. Antiskyrmions may have been observed in materials with the D_{2d} symmetry class,²⁴ and have $m = -1$ (it should be noted that, although making the inversion of the position coordinates $\mathbf{r} \rightarrow -\mathbf{r}$ flips the sign of N_{sk} , we refer to antiskyrmions as specifically the structure with $m = -1$ in this work). Unlike Bloch and Néel skyrmions which have a homochiral structure, antiskyrmions exhibit multichirality, with a Bloch-type profile along the

$\phi = 0$ line and a Néel-type profile along the $\phi = \pi/4$ line, as shown in the bottom-right of Fig. 2. While a global shift in η transforms the structure between Bloch and Néel states for a skyrmion with $N_{\text{sk}} = 1$, the same transformation applied to an antiskyrmion merely rotates it about its centre.

1.3. (Anti-)skyrmion Dynamics and Applications

Since it was first observed in the 1960s, Moore's law, stating that the number of transistors on a chip approximately doubles every 18 months, predicts an exponential increase in processing power.²⁵ However, this law is beginning to fail firstly, in part, due to the increasing level of heat dissipation on an increasingly dense chip.²⁶ Secondly, as the size of transistors approaches the atomic scale, the increased prevalence of quantum tunnelling will result in the devices becoming impractical.²⁷ In addition to these limits on current information processing technology, there are similar limits on our current information storage devices. Solid-state drives, which use transistors to store information, encounter the same problems. In hard disk drives, which use magnetic domains to store data, the process of flipping the magnetisation of entire magnetic domains dissipates a significant amount of heat.²⁸

The use of magnetic skyrmions in information processing and data storage devices has been proposed to overcome these problems. In both cases, the skyrmions are driven along a track, often by a spin-polarised current. The low current density needed to drive skyrmions means that much less energy would be required in their operation than with conventional devices, in addition to the skyrmions' small size, allowing for high densities of information carriers, and topological stability, allowing low-loss information processing and storage.²⁹ An example of the use of skyrmions in a memory device is in skyrmion-based racetrack memory devices, illustrated in Fig. 3. Originally imagined in the context of moving domain walls,³⁰ such a device would operate by driving skyrmions along a nanotrack using a spin-polarised current.³¹ The presence or absence of a skyrmion would then correspond to a binary digit.

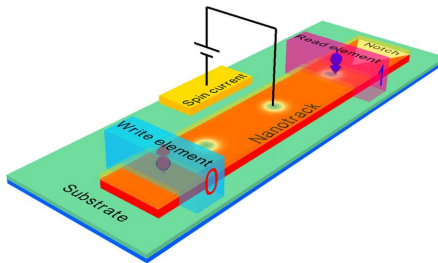


FIG. 3: Schematic of a skyrmion-based racetrack memory device. Figure from Ref. 32.

In this work, we study the dynamics of antiskyrmions, which are potentially a more promising candidate for such applications of skyrmions. When a spin-polarised current is injected into a magnetic system containing skyrmions, the skyrmion gains a component of velocity in the direction of the current, as well as a component in the transverse direction, a phenomenon

known as the skyrmion Hall effect, which can result in loss of data as skyrmions collide with the boundary of the track.³³ In the case of antiskyrmions, this effect can be eliminated with a specific orientation of an applied magnetic field.³⁴ Additionally, antiskyrmions can be realised above room temperature, and offer increased stability over skyrmions due to dipolar interactions.²⁸ The resonance dynamics of antiskyrmions have not been well-classified, and in this work, we aim to shed some light on this subject.

2. MICROMAGNETICS

In our work, we use micromagnetic simulations to predict the behaviour of magnetic systems. In order to simulate large-scale systems (where the configurations of interest are on a scale much larger than that of a lattice unit cell), we must discretise the system, such that domains of the sample containing many magnetic moments are replaced by a single magnetic moment, considered to be the average of the unit magnetic moments within it. The two main assumptions made in using micromagnetic models are:³⁵

- The magnetisation vector field $\mathbf{M}(\mathbf{r}, t)$ is continuous and slowly-changing in time and space.
- The magnitude of the magnetisation $M_s = |\mathbf{M}|$ is constant, such that it may be written as $\mathbf{M} = M_s \mathbf{m}$, where $|\mathbf{m}| = 1$.

There are two widely-used methods in micromagnetic modelling: the finite-difference and the finite-element methods. In the finite-difference method, the system is divided into many cuboids, each with a single magnetic moment that reflects the average of the many magnetic moments it contains. On the other hand, in the finite-element method, the system is divided into many tetrahedra, again, each with a magnetic moment. The discretisation should be sufficiently small that each element is smaller than the magnetic exchange length

$$l_{\text{ex}} = \sqrt{\frac{2A}{\mu_0 M_s^2}}, \quad (6)$$

which measures the relative strength of exchange and self-magnetostatic energies,³⁶ as well as the helical length³⁷

$$l_h = \frac{4\pi A}{|D|}, \quad (7)$$

which is the wavelength of a magnetic helix when the material is in the helical state.

Simulations typically use Neumann or periodic boundary conditions. Neumann boundary conditions may be obtained by the minimisation of the energy functional to give a set of differential equations that describe the edge effects in the magnetisation field,³⁸ while periodic boundary conditions may be treated by considering the simulation system being repeated a number of times along some or all orthogonal axes of the sample.³⁹

In 1935, L. Landau and E. Lifshitz derived an equation for the change in \mathbf{m} over time in the absence of damping:⁴⁰

$$\dot{\mathbf{m}} = -\gamma_0 \mathbf{m} \times \mathbf{H}_{\text{eff}}, \quad (8)$$

where $\gamma_0 = \gamma\mu_0$, the product of the gyromagnetic ratio of the electron and the permeability of free space, and \mathbf{H}_{eff} is the effective magnetic field. In 1955, T. L. Gilbert introduced a phenomenological damping parameter α ⁴¹ to give the Landau-Lifshitz-Gilbert (LLG) equation:

$$\dot{\mathbf{m}} = -\gamma_0^* \mathbf{m} \times \mathbf{H}_{\text{eff}} + \alpha \mathbf{m} \times \dot{\mathbf{m}}, \quad (9)$$

where $\gamma_0^* = \gamma_0(1 + \alpha^2)$ is the modified gyromagnetic ratio. The effective magnetic field is given by the functional derivative

$$\mathbf{H}_{\text{eff}} = -\frac{1}{\mu_0 M_s} \frac{\delta E[\mathbf{m}]}{\delta \mathbf{m}}, \quad (10)$$

where $E[\mathbf{m}]$ is the energy functional of the system, discussed in Section 3.

Throughout this work, we use the finite-difference micromagnetic simulation software `mumax`^{3,42} modified to include the anisotropic DMI,³⁷ described in Section 3.2.

3. MAGNETIC INTERACTIONS

The total energy functional is given by the integral of the energy densities from various energy contributions over the volume of the sample,

$$E[\mathbf{m}] = \int_V d^3r [w_{\text{ex}}(\mathbf{r}) + w_{\text{dmi}}(\mathbf{r}) + w_a(\mathbf{r}) + w_z(\mathbf{r}) + w_d(\mathbf{r})], \quad (11)$$

where $w_{\text{ex}}(\mathbf{r})$ is the symmetric exchange energy density, $w_{\text{dmi}}(\mathbf{r})$ is the Dzyaloshinskii-Moriya interaction energy density, $w_a(\mathbf{r})$ is the uniaxial anisotropy energy density, $w_z(\mathbf{r})$ is the Zeeman interaction energy density, and $w_d(\mathbf{r})$ is the energy density resulting from interaction of the magnetic moments with the demagnetising field. We can obtain the parameters associated with each term experimentally,^{24,43} or theoretically through the use of density functional theory.^{44,45} The following sections discuss the origins of each term.

3.1. Symmetric Exchange Energy

The symmetric exchange term results from the fact that the wavefunction of two electrons in a given energy state must be antisymmetric with respect to the exchange of two electrons, resulting in an electrostatic interaction between them. In 1926, W. Heisenberg proposed the following model for the energy of the exchange interaction:⁴⁶

$$E_{\text{ex}} = -J \sum_{\langle i, j \rangle} \mathbf{S}_i \cdot \mathbf{S}_j, \quad (12)$$

which is a sum of the nearest-neighbour interactions between spins in the system \mathbf{S}_i , assuming a constant exchange integral J . Within the continuum approximation assumed in micromagnetics, where all spins have the same magnitude S and there are n atoms within a unit cell of a cubic lattice with lattice constant a , it is possible to derive the energy density⁴⁷

$$w_{\text{ex}} = A(\nabla \mathbf{m})^2, \quad (13)$$

where $A = JS^2n/a$ is the exchange stiffness constant. This gives a contribution to the effective field of

$$\mathbf{H}_{\text{eff, ex}} = \frac{2A}{\mu_0 M_s} \nabla^2 \mathbf{m}. \quad (14)$$

3.2. Dzyaloshinskii-Moriya Energy

The Dzyaloshinskii-Moriya interaction, also known as the antisymmetric exchange interaction, appears in magnetic systems where there is a lack of inversion symmetry. This can appear in bulk due to a noncentrosymmetric crystal structure, or at an interface between two different materials, which inherently breaks inversion symmetry. It was first introduced in 1958 by I. Dzyaloshinskii through an analysis of the crystal structure symmetry,⁴⁸ and explained microscopically by T. Moriya through an extension of the theory of superexchange to include spin-orbit coupling.⁴⁹ The Dzyaloshinskii-Moriya energy between spins \mathbf{S}_i and \mathbf{S}_j is given by

$$E_{\text{dmi}} = \mathbf{D}_{ij} \cdot (\mathbf{S}_i \times \mathbf{S}_j), \quad (15)$$

where \mathbf{D}_{ij} is the Dzyaloshinskii-Moriya vector, which is constrained by symmetry rules. This interaction favours the situation where \mathbf{S}_i , \mathbf{S}_j , and \mathbf{D}_{ij} are mutually perpendicular. An example of a system which would exhibit this interaction is shown in Fig. 4.

The notation of Lifshitz invariants are often used in discussions of the DMI, which have the

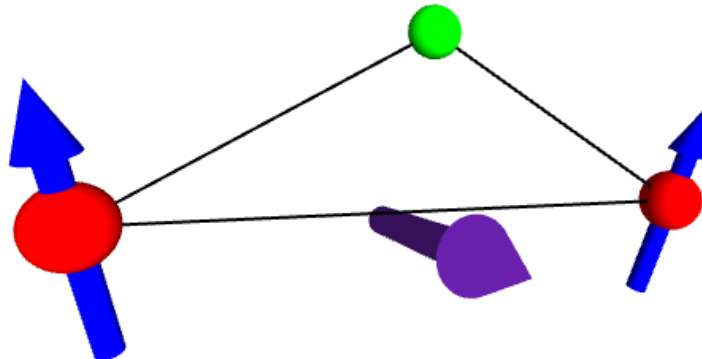


FIG. 4: Example of a system lacking inversion symmetry that would display the Dzyaloshinskii-Moriya interaction. Two ions with magnetic moments (red) are coupled to a third ion (green) via the superexchange mechanism, resulting in a DMI with a DM vector shown in purple.

Figure recreated from Ref. 50.

form

$$\mathcal{L}_{ij}^{(k)} = m_i \partial_k m_j - m_j \partial_k m_i. \quad (16)$$

This allows the symmetry constraints to be expressed in terms of a single parameter D , the DMI strength.

Depending on the geometry of the broken symmetry, the expression for the DMI energy density can have different forms.³⁷ For a material with a T or O symmetry class, the DMI energy density is given by

$$w_{\text{DMI}} = D(\mathcal{L}_{zy}^{(x)} + \mathcal{L}_{xz}^{(y)} + \mathcal{L}_{yx}^{(z)}) = D\mathbf{m} \cdot (\nabla \times \mathbf{m}). \quad (17)$$

If the system is a thin film with interfacial DMI, or a crystal with symmetry class C_{nv} , with $n > 2$, located in the $x - y$ plane, the energy density is given by:

$$w_{\text{DMI}} = D(\mathcal{L}_{xz}^{(x)} + \mathcal{L}_{yz}^{(y)}) = D(\mathbf{m} \cdot \nabla m_z - m_z \nabla \cdot \mathbf{m}). \quad (18)$$

If the crystal has the symmetry class D_{2d} , the DMI energy density is

$$w_{\text{DMI}} = D(\mathcal{L}_{xz}^{(y)} + \mathcal{L}_{yz}^{(x)}) = D\mathbf{m} \cdot (\partial_x \mathbf{m} \times \hat{x} - \partial_y \mathbf{m} \times \hat{y}). \quad (19)$$

For the case of the D_{2d} symmetry that stabilises antiskyrmions, the effective field is given by

$$\mathbf{H}_{\text{eff, DMI}} = \frac{D}{\mu_0 M_s} (\partial_y \mathbf{m} \times \hat{y} - \partial_x \mathbf{m} \times \hat{x}). \quad (20)$$

3.3. Uniaxial Anisotropy Energy

A combination of spin-orbit coupling and the interaction of electron orbits with the crystal field can result in the magnetisation tending to align along directions which are more energetically-favourable (easy axes), an effect known as magnetocrystalline anisotropy. If there is only a single easy axis \hat{u} , this is known as uniaxial anisotropy. The case of uniaxial anisotropy usually holds for most materials, as higher-order energy terms are negligible.^{51,52} This has the energy density

$$w_a = -K_u (\mathbf{m} \cdot \hat{u})^2, \quad (21)$$

where K_u is the anisotropy constant. This results in the contribution to the effective field

$$\mathbf{H}_{\text{eff, a}} = \frac{2K_u}{\mu_0 M_s} \mathbf{m} \cdot \hat{u}. \quad (22)$$

In practice, contributions of anisotropy to the system's energy are often neglected in micromagnetic simulations as it usually does not have a great effect on the dynamics of the system compared to other energy contributions.^{24,35,53}

3.4. Zeeman Interaction Energy

Magnetic moments tend to align along the direction of an applied field \mathbf{H}_{app} , which results in the Zeeman energy density contribution

$$w_z = -\mu_0 M_s \mathbf{m} \cdot \mathbf{H}_{\text{app}}. \quad (23)$$

The contribution to the effective field is simply the applied field,

$$\mathbf{H}_{\text{eff}, z} = \mathbf{H}_{\text{app}}. \quad (24)$$

3.5. Demagnetisation Energy

For a system of many discrete (atomistic) spins, there is an energy contribution due to the combined dipolar field experienced by each spin from every other spin in the system, analogous to the Zeeman interaction energy described in the previous section. By applying Maxwell's equations to the system in the continuum approximation, it can be shown⁵⁴ that the demagnetising field resulting from the dipolar field within the continuum approximation \mathbf{H}_d can be written in terms of a vector potential Φ_M ,

$$\mathbf{H}_d = -\nabla\Phi_M, \quad (25)$$

where Φ_M satisfies the Poisson equation

$$\nabla^2\Phi_M = \nabla\mathbf{M}. \quad (26)$$

The energy contribution from the demagnetising field can be expressed as an integral over the volume of the sample,

$$E_d = \frac{1}{2}\mu_0 M_s \int_V d^3r \mathbf{m} \cdot (\nabla\Phi_M). \quad (27)$$

The demagnetisation energy density contribution is given by

$$w_d = -\frac{1}{2}\mu_0 M_s \mathbf{m} \cdot \mathbf{H}_d, \quad (28)$$

and the corresponding effective field contribution is expressed as the convolution

$$\mathbf{H}_{\text{demag}, i} = \hat{\mathbf{K}}_{ij} * \mathbf{m}_j, \quad (29)$$

where $\hat{\mathbf{K}}_{ij}$ is a demagnetisation kernel that can be evaluated using a variety of methods.⁵⁵

4. RESONANCE CALCULATIONS

An understanding of the dynamical properties of skyrmions and antiskyrmions is important in order to understand their stability, as well as to understand how they can be manipulated. A rigid spin texture is often assumed in predicting the behaviour of skyrmions, for example, under the injection of a spin-polarised current, but understanding the richer dynamics when this assumption is lifted can give us more information that may be used in the design of skyrmionic devices. For example, it has been suggested that the antiskyrmion velocity under the injection of a spin-polarised current is greatest when the perpendicular isotropy oscillates (from the application of an electric field) at the resonant frequency.³⁴ Despite the important implications of antiskyrmion resonance modes, there have been no experimental studies on the matter, while theoretical and computational studies are limited.

4.1. Ringdown Method

In the ringdown method, we begin by relaxing the system to its ground state \mathbf{m}_0 . We then apply a time-dependent external magnetic field $\mathbf{h}(t) = h_{\max} \operatorname{sinc}(2\pi f_c t)\hat{\mathbf{e}}$, where $\hat{\mathbf{e}}$ is the direction of the applied perturbing magnetic field, for a time t_{app} .⁵³ Fig. 5 shows that this form of the excitation field results in the eigenmodes with a frequency less than the cutoff frequency f_c being excited approximately equally, each with an amplitude of $H^f \approx h_{\max}/2f_c t_{\text{app}}$. The signal reaches its peak at some time t_0 . Once the field is removed, the sampling of the magnetic moment configuration is delayed by some time t_{del} in order to avoid the introduction of nonlinearities into the system's dynamics. Sampling occurs over a time t_{samp} , during which the magnetisation of each cell is recorded at times $t_j = j\Delta t$, where Δt is the time between samples and $j \in \mathbb{N}$. We then perform a Fourier analysis on the resulting oscillations, as described in the following section.

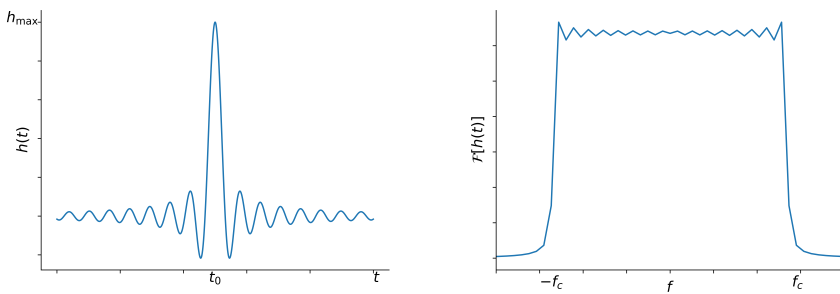


FIG. 5: Left: The cardinal sine wave excitation used in the ringdown method. Right: The Fourier transform of the perturbing field, demonstrating that the eigenmodes are excited with approximately equal amplitude.

4.2. Fourier Analysis

In order to analyse the magnetisation dynamics of a system which has been perturbed from equilibrium, for example by applying a magnetic field pulse as described in the previous section, or by initialising the system away from its equilibrium position, we perform a Fourier analysis on the time-dependent part of the magnetisation vector field, $\Delta\mathbf{m}(\mathbf{r}_k, t_l) = \mathbf{m}(\mathbf{r}_k, t_l) - \mathbf{m}_0(\mathbf{r}_k)$. For this, we use the spatially-resolved power spectral density⁵⁶

$$P_{\text{sr}} = \frac{1}{N} \sum_{j=x,y,z} \sum_{k=1}^N \left| \sum_{l=1}^n \Delta m_j(\mathbf{r}_k, t_l) e^{-2\pi i f t_l} \right|^2, \quad (30)$$

where N is the number of elements of the sample and n is the number of times at which the magnetisation is sampled.

4.3. Eigenvalue Method

A method for the calculation of resonance modes in magnetic systems was introduced by d'Aquino in 2009.⁵⁷ We consider perturbations from the magnetisation ground state $\mathbf{m}_0(\mathbf{r})$ of the form $\mathbf{m}(\mathbf{r}, t) = \mathbf{m}_0(\mathbf{r}) + \epsilon \mathbf{v}(\mathbf{r}, t)$, where $\epsilon \in \mathbb{R}^+$ and the condition that $|\mathbf{m}| = 1$ implies that $\mathbf{v}(t) \perp \mathbf{m}_0$ (we will drop the explicit \mathbf{r} -dependence of the vector fields for the rest of this section for simplicity). We can expand the effective field as $\mathbf{H}_{\text{eff}}[\mathbf{m}_0 + \epsilon \mathbf{v}(t)] = \mathbf{H}_{\text{eff}}(\mathbf{m}_0) + \epsilon \mathbf{H}'_{\text{eff}}(\mathbf{m}_0) + \mathcal{O}(\epsilon^2)$ and substitute this into the Eq. 9 to obtain in the undamped limit to obtain⁵³

$$\dot{\mathbf{v}}(t) = -\gamma_0^* \{ \mathbf{v}(t) \times \mathbf{H}_0 + \mathbf{m}_0 \times [\mathbf{H}'_{\text{eff}}(\mathbf{m}_0) \cdot \mathbf{v}(t)] \}, \quad (31)$$

where $\mathbf{H}_0 = \mathbf{H}_{\text{eff}}(\mathbf{m}_0)$ and $\mathbf{H}'_{\text{eff}}(\mathbf{m})$ is the rank-2 tensor $\nabla_{\mathbf{m}} \mathbf{H}_{\text{eff}}(\mathbf{m})$. As $\mathbf{H}_{\text{eff}}(\mathbf{m}_0) \parallel \mathbf{m}_0$ and $|\mathbf{m}_0| = 1$, we can write $\mathbf{H}_0 = h_0 \mathbf{m}_0$, where h_0 is the scalar field $h_0 = |\mathbf{H}_0|$, to obtain the equation

$$\dot{\mathbf{v}}(t) = \gamma_0^* \mathbf{m}_0 \times \{ [h_0 \mathbf{I} - \mathbf{H}'_{\text{eff}}(\mathbf{m}_0)] \cdot \mathbf{v}(t) \}, \quad (32)$$

where \mathbf{I} is the $3N \times 3N$ identity matrix, where the sample has N discretisation cells. We then define the matrix $\Lambda(\mathbf{m}_0)$ such that $\mathbf{m}_0 \times \mathbf{x} = \Lambda(\mathbf{m}_0) \cdot \mathbf{x}$ and write the solutions of the differential equation as $\mathbf{v}(t) = \tilde{\mathbf{v}} e^{2\pi i f t}$ to obtain the eigenvalue equation

$$2\pi i f \tilde{\mathbf{v}} = A \tilde{\mathbf{v}}, \quad (33)$$

where $A = \gamma_0^* \Lambda(\mathbf{m}_0) [h_0 \mathbf{I} - \mathbf{H}'_{\text{eff}}(\mathbf{m}_0)]$. This equation can then be solved for the eigenfrequencies f .

5. RESONANCES OF AN ANTISKYRMION IN A NANODISK

5.1. Introduction

We begin with the relatively simple system of an antiskyrmion in a nanodisk. It has been shown that for a nanodisk, a skyrmionic spin texture is the state of lowest energy at zero field and in the absence of magnetocrystalline anisotropy,⁵⁸ making this an ideal starting point for these investigations. Our investigation of this system is based on a similar investigation by Beg et. al. in which the dynamics of Bloch skyrmions in a nanodisk are investigated,⁵³ and, as such, we use the same parameters, but instead using the anisotropic DMI characteristic to materials with a D_{2d} crystal structure. These parameters are a saturation magnetisation $M_s = 384 \text{ kA m}^{-1}$, an exchange stiffness $A = 8.78 \text{ pJ m}^{-1}$, and a DMI strength $D = 1.58 \text{ mJ m}^{-2}$. Furthermore, as in the work with Bloch skyrmions, we assume that the material is isotropic, allowing us to neglect any terms resulting from anisotropy in the effective field. Whilst we are not simulating any particular material, our parameters are of the order of magnitude of those for systems in which antiskyrmions are observed.^{24,59} We choose the diameter of our nanodisk $d = 150 \text{ nm}$, and thickness $t = 150 \text{ nm}$. We simulate the system using `mumax3`, in which we discretise the system in cuboids of $3 \text{ nm} \times 3 \text{ nm} \times 2 \text{ nm}$, which is much less than $l_{\text{ex}} \approx 10 \text{ nm}$ and $l_h \approx 70 \text{ nm}$. Relaxing this system gives a spin texture with a skyrmion number $N_{\text{sk}} = -0.89$, which is close to the expected value for an antiskyrmion of -1 . Unlike for quasi-infinite magnetic textures, the skyrmion number is not an integer for (anti-)skyrmions in confined magnetic textures.^{58,60}

In order to perform the ringdown method on the system, we seed the initial state by starting with $\mathbf{m} = (0, 0, -1)$ for a region of radius $d/4$ in the centre of the disk and $\mathbf{m} = (0, 0, 1)$ elsewhere. We relax the system with the high damping constant of $\alpha = 1$ in order to reduce the time required for the system to relax. During the rest of the simulation, we use a much lower

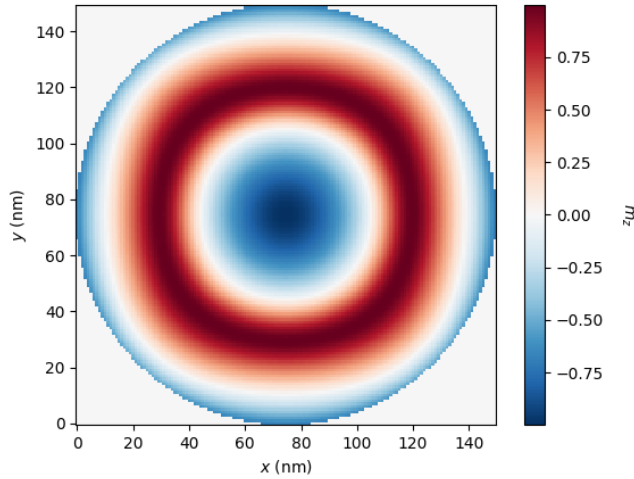


FIG. 6: The z -component of magnetisation of a relaxed antiskyrmion in a nanodisk of diameter $d = 150 \text{ nm}$.

damping constant of $\alpha = 0.002$. We use a pulse with a maximum amplitude $h_{\max} = 50\text{ mT}$, and a cutoff frequency $f_c = 100\text{ GHz}$. We choose to only examine modes of eigenfrequencies up to 50 GHz in order to avoid aliasing due to the finite time sampling.⁶¹ When examining in-plane modes, we set the direction of the perturbing field to be along the x -axis, in the plane of the antiskyrmion, and for the out-of-plane modes, the field is along the z -axis, orthogonal to the plane of the antiskyrmion. As explained in Section 4.1, each mode is excited approximately equally with an amplitude of $H^f \approx 0.5\text{ mT}$. We apply the pulse for a time $t_{\text{app}} = 0.5\text{ ns}$, with a peak at $t_0 = 0.25\text{ ns}$. We delay the sampling for a time $t_{\text{del}} = 2\text{ ns}$, and sample over a time $t_{\text{samp}} = 20\text{ ns}$, at time intervals of $\Delta t = 5\text{ ps}$.

In order to visualise the modes, we apply an oscillating magnetic field to the sample of the form $\mathbf{h}(t) = H^f \sin(2\pi f_{\text{ex}}t)\hat{\mathbf{e}}$, where $H^f = 0.5\text{ mT}$, f_{ex} is the excitation frequency determined using the ringdown method, and $\hat{\mathbf{e}}$ is either \hat{x} , in the plane of the antiskyrmion for in-plane excitations, or \hat{z} , orthogonal to the plane of the antiskyrmion for out-of-plane excitations. The simulation is run for several times periods of the mode, in order to ensure that the excitations are sufficient that they can be viewed clearly. As the excitations are barely visible when we simply show m_z , we enhance the resonances by some factor k , such that we plot $m_{z0} + k[m_z(t) - m_{z0}]$. In this section, $k = 100$. Throughout this work, we show the resonance modes over an entire period of oscillation T , in intervals of $T/8$, across the page.

5.2. Comparison of Finite-Difference and Finite-Element Simulations

Given that our system has a circular geometry, it is intuitively clear that the finite-difference discretisation will result in discrepancies compared to an ideal system in which the edges are perfectly smooth. However, it is more practical for us to use `mumax3` for our simulations as it is GPU-accelerated, allowing us to run simulations much more quickly ($\sim 100\times$ the speed of CPU-based simulations).⁴² In order to justify our use of this software over finite-element software such as `Finmag`, we test the case of the ringdown simulations of an antiskyrmion in a circular nanodisk modelled using the finite-difference software `mumax3` against the results obtained using the finite-element software `Finmag`.

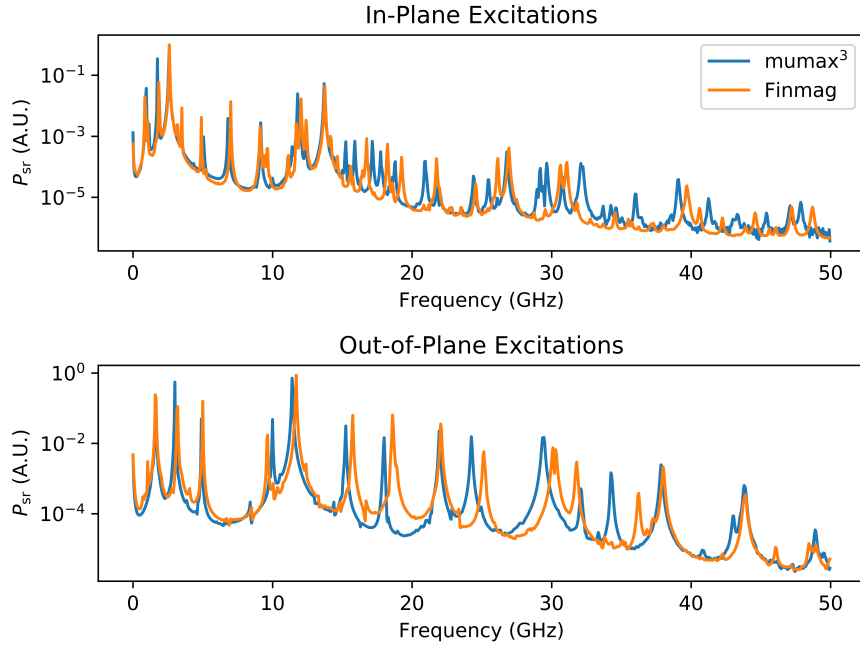


FIG. 7: Comparison of the spatially-resolved power spectral densities of an antiskyrmion in a nanodisk for the finite-difference software mumax^3 and the finite-element software Finmag for in-plane excitations (top) and out-of-plane excitations (bottom).

Fig. 7 shows that both methods give very similar power spectra, which indicates that our assumption that we may use finite-difference modelling to simulate the antiskyrmion in a nanodisk is justified. In order to further justify this, we carried out simulations using each of the software packages for a range of frequencies and found that sine-wave oscillations applied to the sample at corresponding frequencies for each of the packages gave rise to the same qualitative behaviour.

5.3. Comparison of the Ringdown and Eigenvalue Methods

To calculate the eigenfrequencies of the antiskyrmion confined in a nanodisk using the eigenvalue method, we seed the initial state as usual and relax the system such that the components of \mathbf{m} at any point in the sample do not change by more than 10^{-6} within each iteration of the LLG equation solver.

In order to directly compare the resonance frequencies obtained using the ringdown and eigenvalue methods, we plot the sum of the power spectra obtained using the ringdown method in Finmag by both in-plane and out-of-plane excitations in Fig. 8, so that the peaks from both cases are shown, as well as the eigenfrequencies.

A significant disadvantage of the use of the ringdown method in the prediction of eigenfrequencies of Bloch skyrmions in nanodisks is that it often predicts fewer modes than the eigenvalue method. In contrast, our results in Fig. 8 shows that we have excited nearly all of the

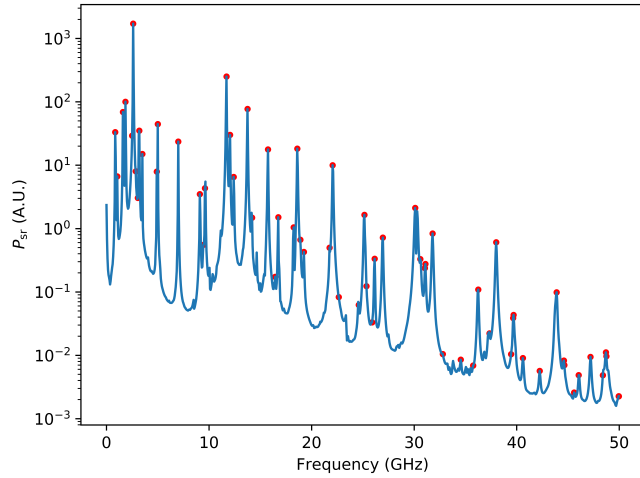


FIG. 8: The sum of the in-plane and out-of-plane spatially-resolved power spectral densities obtained using the ringdown method in Finmag (blue line), and the eigenvalues obtained using the eigenvalue method on the ground state (red dots).

available eigenmodes predicted by the eigenvalue method. There are, however, other significant disadvantages of the ringdown method over the eigenvalue method, such as the possibility of missing distinct modes that are very close together in the spectrum, and the high amount of computing power required to obtain a spectral resolution comparable to that obtained by the eigenvalue method.⁵¹ However, we continue to use the ringdown method in order to obtain the eigenvalues in the remainder of our work as the eigenvalue method is highly nontrivial to implement and, despite a significant degree of effort, we were unable to implement it such that we could apply it to our systems relaxed using mumax³.

5.4. Behaviour of the Modes

The spatially-resolved power spectral densities resulting from the procedure described in the previous section are shown in Fig. 9. Due to the richness of the spectra, we limit ourselves in this work to the discussion of the more intense peaks that are visible without the logarithmic scaling of the P_{sr} -axis, which would be of higher significance experimentally.

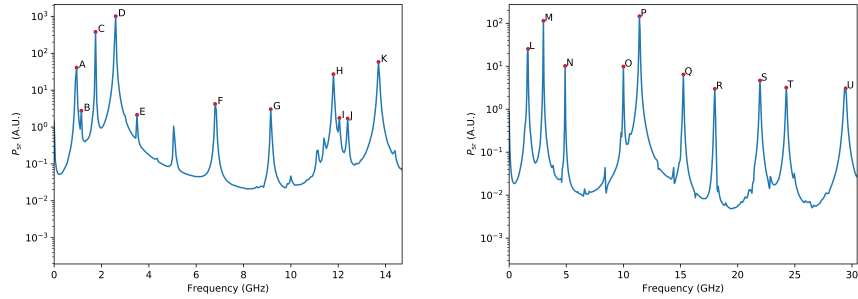


FIG. 9: The spatially-resolved power spectral densities resulting from in-plane excitations (left) and out-of-plane excitations (right) of an antiskyrmion in a nanodisk.

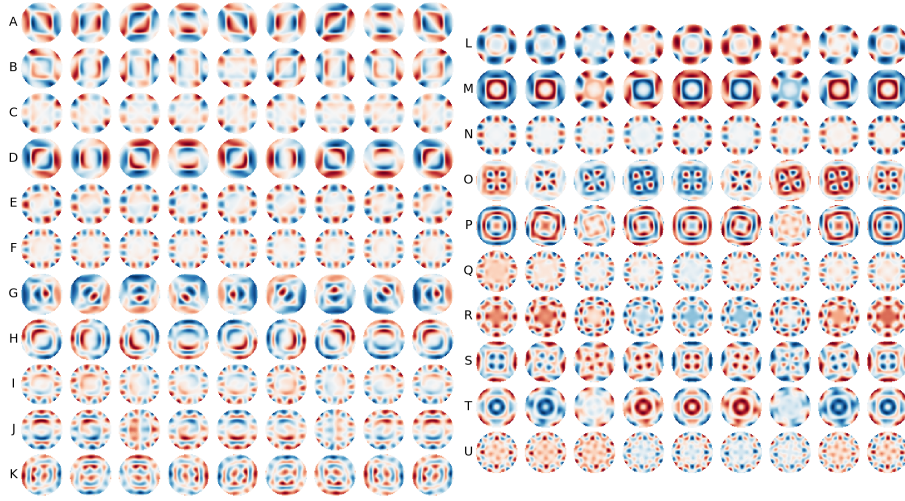


FIG. 10: Eigenmodes of an antiskyrmion in a nanodisk resulting from in-plane excitations (left) and out-of-plane excitations (right).

In comparison to the eigenmodes of Bloch and Néel skyrmions, antiskyrmion modes display relatively complex behaviour, making it difficult to categorise the modes into breathing, rotational, and gyroscopic modes, as often done in the literature.^{53,62,63} The reason for this is unclear, but it is likely due to the multichirality of the spin texture, in contrast to the homochirality of Bloch and Néel skyrmions. We note that, as with Bloch and Néel skyrmions, the resonances corresponding to out-of-plane excitations tend to display behaviour more closely associated with breathing modes, whilst those corresponding to in-plane excitations are more rotational in character.

The most intense mode resulting from in-plane excitations in this system is mode D in the left-hand side of Fig. 10, at 2.60 GHz. This is a relatively simple mode in which the positive and negative deviations in m_z from the ground state are symmetric with respect to a 180° rotation about the centre, and they rotate around the centre at the driving frequency.

The most intense mode resulting from out-of-plane excitations is mode P on the right-hand side of Fig. 10, at 11.40 GHz. This exhibits both breathing and rotational behaviour. In

terms of breathing behaviour, two contour rings in m_z are observed, which oscillate mutually out-of-phase. In terms of rotational modes, a pattern of four-fold symmetry of alternating positive and negative displacements of m_z from the equilibrium texture rotates clockwise close to and about the centre. Meanwhile, the deviations near the edges display a similar symmetry but rotate in an anticlockwise fashion, and the deviations about the maximum- m_z “square” are displaced slightly by a small amount clockwise, then anticlockwise, over the course of the time period corresponding to this frequency.

5.5. Effect of Saturation Magnetisation on Resonance Modes

A notable feature of an antiskyrmion confined in a nanodisk is the square shape which can be seen in Fig. 6, which is in contrast to the uniform circular symmetry seen for Bloch and Néel skyrmions confined in nanodisk. An explanation of this is that, above a certain M_s , the structure transitions into that shown in Fig. 6 to promote the Bloch-like rotations along the diagonals, which cost less dipolar energy than Néel-type rotations.⁶⁴ In contrast, below this “transition”, we see a ground state with a different structure, as shown in Fig. 11.

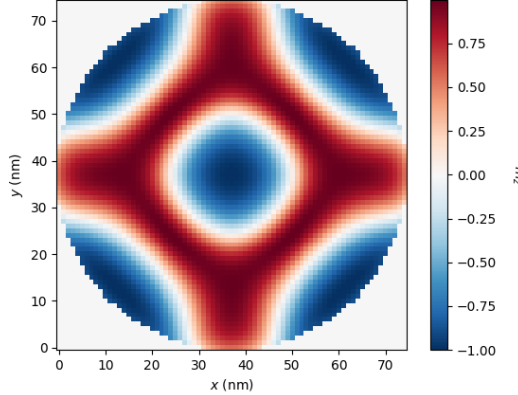


FIG. 11: The ground state of a nanodisk with anisotropic DMI for a low M_s .

One would expect that, by virtue of this difference, we would observe a clear transition in the P_{sr} spectrum for in-plane excitations, shown in Fig. 12. However, we instead see a continuous spectrum.

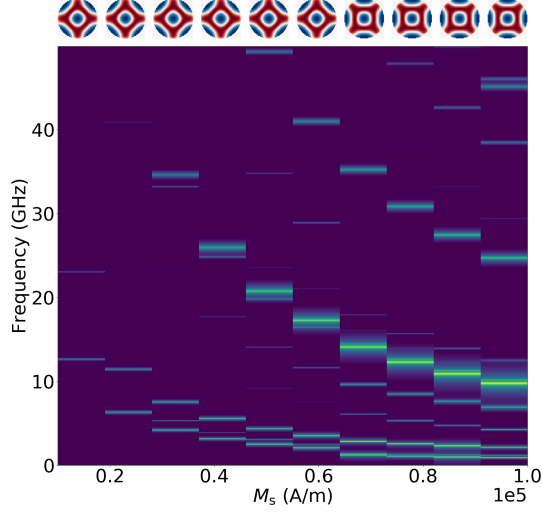


FIG. 12: The variation of the spatially-resolved power spectral density for in-plane excitations as a function of M_s . The structure of m_z for each M_s is shown above.

In order to look at this drastic change in structure in more detail, we directly compare the spatially-resolved power spectra and resonance modes of the system with $M_s = 6 \times 10^4 \text{ Am}^{-1}$ and $M_s = 7 \times 10^4 \text{ Am}^{-1}$, shown side-by-side in Fig. 13.

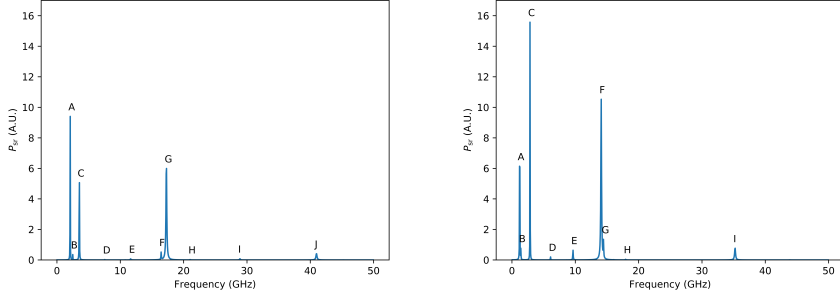


FIG. 13: Power spectral densities for in-plane excitations of the antiskyrmion spin texture confined in a nanodisk for $M_s = 6 \times 10^4 \text{ Am}^{-1}$ (left) and $M_s = 7 \times 10^4 \text{ Am}^{-1}$ (right).

Fig. 14 shows the corresponding modes from the peaks in Fig. 13 side-by-side. We see that the modes are approximately the same, and rotated 45° clockwise with the texture.

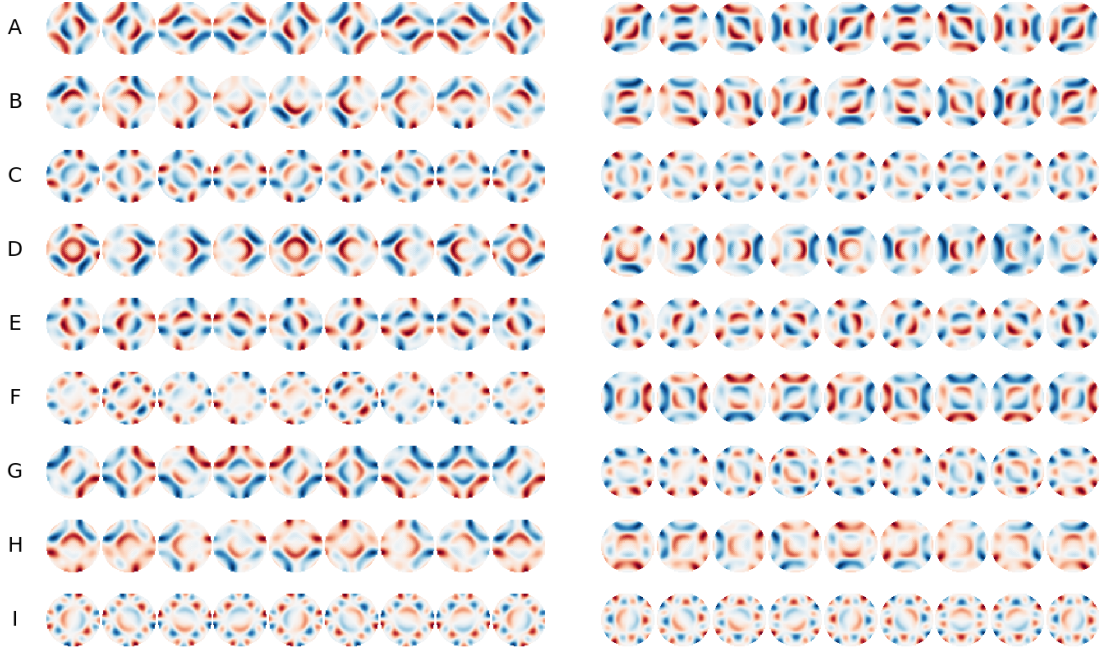


FIG. 14: Resonance modes for the peaks shown in Fig. 13. Left: $M_s = 6 \times 10^4 \text{ Am}^{-1}$, right: $M_s = 7 \times 10^4 \text{ Am}^{-1}$.

6. RESONANCES OF ANTISKYRMIONS IN A LATTICE

6.1. Introduction

A natural extension to the work of the previous section is to examine the resonance modes of antiskyrmions arranged in a lattice. This is useful as lattices of (anti-)skyrmions can form from helical states under certain conditions.^{15,16,24,65} In this work, we use material parameters determined experimentally by Nayak et. al. for $\text{Mn}_{1.4}\text{Pt}_{0.9}\text{Pd}_{0.1}\text{Sn}$.²⁴ These are $A = 120 \text{ pJ m}^{-1}$, $D = 6.0 \text{ mJ m}^{-2}$, $M_s = 445 \text{ kA m}^{-1}$. As with the case of the antiskyrmion in a nanodisk, we take the damping constant $\alpha = 1$ during the relaxation step and $\alpha = 0.002$ during the ringdown simulation. We take the thickness of the sample to be $t = 50 \text{ nm}$, which is relatively thin for such a sample, but still physically-realisable,²⁴ in order to minimise the number of cells (and hence the time) required to simulate this system. As shown in Fig. A1 of Appendix A, the thickness of the sample has little effect on the eigenfrequencies. We again use `mumax3` to obtain the results presented in this section. In this case, as we are dealing with 90° edge geometries, the finite-difference paradigm of this package is better-suited to the system than finite-element simulations. We apply the ringdown method and visualise the modes in the same way as for the antiskyrmion in a nanodisk.

We examine resonance modes of antiskyrmions arranged in both square and hexagonal lattices. In each case, we simulate a single unit cell and apply periodic boundary conditions in the x - and y -axes of the plane of the lattice. For the case of a square lattice, we have a unit cell that is

a square of side length L and we seed the initial state by initialising a background of the spin orientated orthogonal to the lattice plane in the direction $(0, 0, 1)$, then defining circular regions of diameter $L/4$ at the corners of the cell. This can then be relaxed to produce an antiskyrmion lattice, shown in the left-hand side of Fig. 15. For a hexagonal lattice, the procedure is similar, but we instead have rectangular cells of dimensions $\frac{1}{\sqrt{3}}L \times L$, and we place a circle at the centre of the cell, in addition to those in the corners which, under periodic boundary conditions, results in a hexagonal structure by simple geometrical considerations, as shown in the right-hand side of Fig. 15.

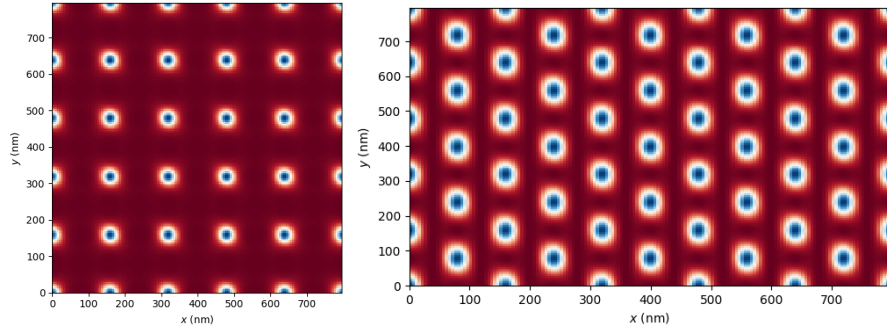


FIG. 15: Left: The relaxed state of our simulated square lattice of antiskyrmions. Right: The relaxed state of our simulated hexagonal lattice of antiskyrmions.

In order to determine L , we keep other parameters fixed and vary L to find the value which minimises the total energy density.⁶⁶ To choose a value for the externally-applied field B_{ext} , we carry out this procedure for values of B_{ext} between 0 T and 1.5 T in increments of 0.1 T and choose values of B_{ext} which are sufficiently high for the antiskyrmions to be far enough apart that their resonance modes are clear, but not so high that the antiskyrmions are either too small to see clearly or destroyed in favour of the conical or spin-polarised state. This results in $B_{\text{ext}} = 0.6$ T and $L = 452$ nm for the square lattice and $B_{\text{ext}} = 0.5$ T and $L = 579$ nm for the hexagonal lattice. In both cases, we discretise our unit cell into $32 \times 32 \times 5$ cuboids, corresponding to approximately 14 nm \times 14 nm \times 10 nm in the case of a square lattice, and 10 nm \times 18 nm \times 10 nm for a hexagonal lattice, which is less than $l_h \approx 250$ nm and $l_{\text{ex}} \approx 30$ nm. That these discretisation sizes are sufficient and yield results very close to those obtained with much smaller discretisation sizes has been confirmed by checking the convergence in $\langle m_z \rangle$ as the discretisation size decreases.

Ideally, we would take the number of repetitions of our unit cell in the x - and y -directions, R , on either side of our unit cell, to be a very high value. However, higher values of R greatly increase the amount of time required to run the simulations due to the amount of time required to calculate the demagnetisation kernel. Therefore, after having determined values for B_{ext} and L using a high value of R , we relax the unit cells for both the square and hexagonal lattices for various values of R between 5 and 100 and calculate the average value of m_z . We note that this converges to a constant value, and we choose $R = 60$ as a trade-off between the accuracy and the speed of the simulations.

As with the case of the nanodisk, we enhance the deviations of \mathbf{m} in our plots by a factor k . In

this section, $k = 1000$.

6.2. Square Lattice Resonance Modes

The power spectrum of the square antiskyrmion lattice is shown in Fig. 16. As with the case of the antiskyrmion in a nanodisk, we limit our discussion to the resonance modes which are visible without the logarithmic scaling of the P_{sr} -axis. We note our method of simulating a single unit cell and the imposition of periodic boundary conditions excludes the possibility of observing lattice modes, i.e. long-ranged excitations in which the antiskyrmions move relative to each other.

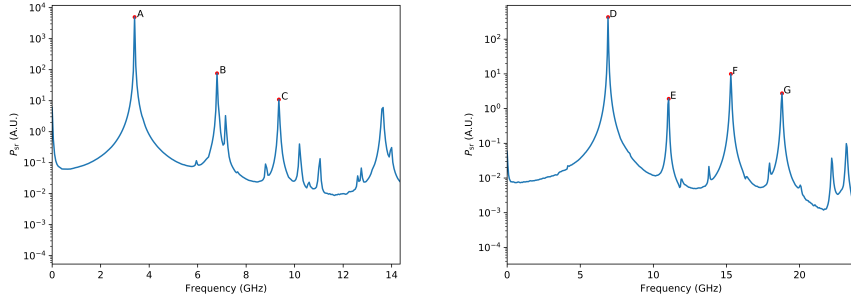


FIG. 16: The power spectral density of in-plane excitations (left) and out-of-plane excitations (right) for the simulated square antiskyrmion lattice.

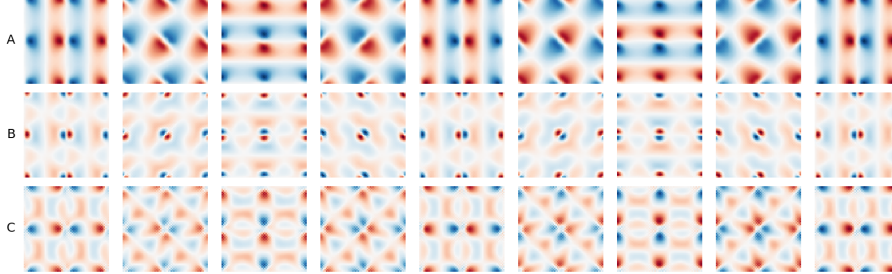


FIG. 17: The excitation modes of the square antiskyrmion lattice for a field applied in the plane of the antiskyrmions, corresponding to the labelled peaks in the left-hand side of Fig. 16.

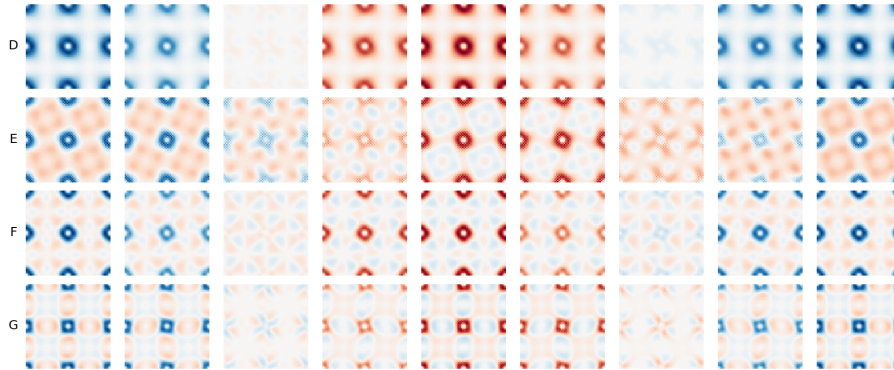


FIG. 18: The excitation modes of the square antiskyrmion lattice for a field applied orthogonal to the plane of the antiskyrmions, corresponding to the labelled peaks in the right-hand side of Fig. 16.

The resonance modes corresponding to the labelled peaks in Fig. 16 are shown in Figs. 17 and 18. As with the previous system, the resonance modes generally become more complicated as the frequency increases. The most intense in-plane excitation is mode A, at a frequency of 3.40 GHz shown in Fig. 17, which consists of two diametrically-opposed lobes rotating anticlockwise in which the deviation of m_z from the ground state is in opposite directions. The in-plane mode B at 6.80 GHz is similar, but the lobes are smaller, and the rotation is clockwise. In-plane mode C at 9.35 GHz is more complex, consisting of a periodic deformation of each antiskyrmion between a two-lobed and four-lobed structure, rotating anticlockwise.

For the out-of-plane excitations, the lowest-frequency mode D, at 6.90 GHz, is again the most intense. This is relatively simple in character, with the m_z of each antiskyrmion oscillating between positive and negative deviations from equilibrium. The other modes E, F, and G, also shown in Fig. 18, are more complicated mixtures of breathing and rotational behaviour.

6.3. Hexagonal Lattice Resonance Modes

In this section, we show the results analogous to those of the previous section, for resonances of antiskyrmions arranged in a hexagonal lattice. Again, as we are simulating a single unit cell and applying periodic boundary conditions, we do not observe any lattice modes.

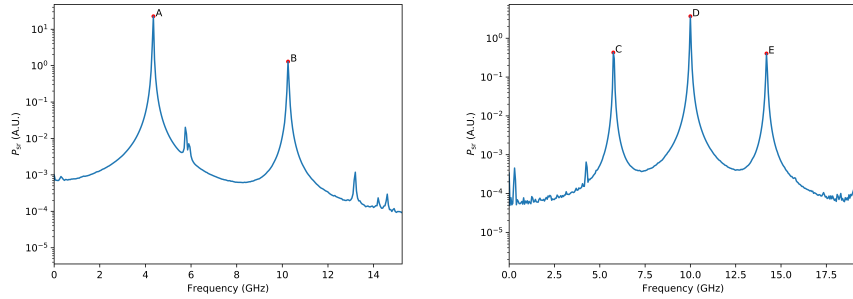


FIG. 19: The power spectral density of in-plane excitations (left) and out-of-plane excitations (right) for the simulated hexagonal antiskyrmion lattice.

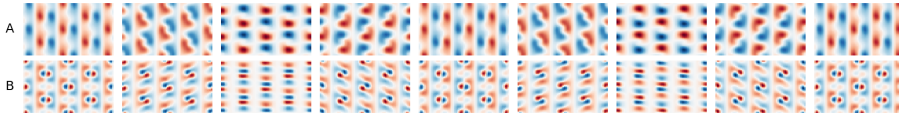


FIG. 20: The excitation modes of the hexagonal antiskyrmion lattice for a field applied in the plane of the antiskyrmions, corresponding to the labelled peaks in the left-hand side of Fig. 19.

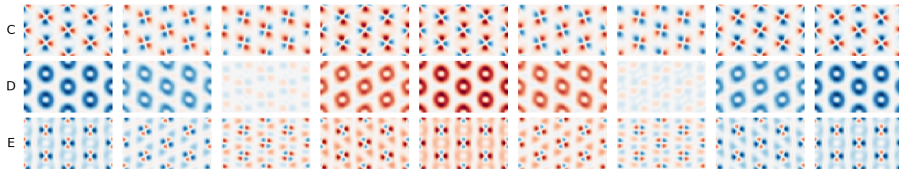


FIG. 21: The excitation modes of the hexagonal antiskyrmion lattice for a field applied orthogonal to the plane of the antiskyrmions, corresponding to the labelled peaks in the right-hand side of Fig. 19.

For in-plane excitations, we observe two significant peaks, the modes of which are shown in Fig. 20, labelled A and B, at 4.35 GHz and 10.25 GHz respectively. The more intense mode A is similar in character to the in-plane mode A for the square lattice, i.e. two diametrically-opposed lobes of opposite m_z deviation from equilibrium rotating anticlockwise. The weaker mode B is similarly comparable to the in-plane mode B of the square lattice. These similarities hint that the structuring of the antiskyrmions may not play a significant role in the resonance behaviours of the antiskyrmions. The large difference in frequencies between the corresponding modes is likely due to the difference in B_{ext} between the two systems. The effect of an increase in the externally-applied magnetic field is generally to increase the resonance frequencies, as shown in Fig. A2 in Appendix B.

For the out-of-plane excitations shown in Fig. 21, we see three major peaks, the most intense being the breathing mode D at 10.00 GHz. Modes C and E at 5.75 GHz and 14.20 GHz respectively are similar in character, with each antiskyrmion resonance possessing two-fold symmetry of alternating lobes of positive and negative deviations of m_z from equilibrium, with the pattern rotating clockwise.

7. DYNAMICS OF ANTISKYRMIONS IN NANOTRACKS

7.1. Introduction

Having previously excluded the possibility of observing lattice modes, we now aim to demonstrate the existence of such modes for a one-dimensional lattice. The results obtained in this section have direct implications for the use of antiskyrmions in the racetrack memory devices described in Section 1.3. We consider the system shown in Fig. 22, a system of six $L \times L$ cells along the x -axis with the same parameters as those used in the simulations of a square antiskyrmion lattice in Section 6.2. In order to approximate a long racetrack, we apply periodic boundary conditions such that the system is repeated five times in either direction along the x -axis.

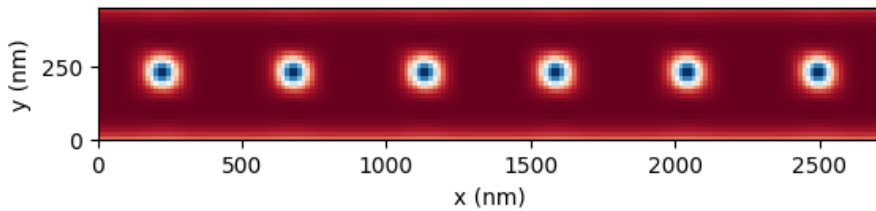


FIG. 22: The z -component of the magnetisation of equally-spaced antiskyrmions in a nanotrack.

7.2. Antiskyrmion-Antiskyrmion Interactions

Whilst some work^{32,67} suggests that the interactions between two skyrmions are purely repulsive, and hence that the system shown in Fig. 22 should be in a stable equilibrium, other work⁶⁸ suggests that skyrmion-skyrmion interactions can be either attractive or repulsive. In order to determine the nature of such interactions in antiskyrmions, we first consider a system with the geometry of such a racetrack, with all magnetic moments along the $(0, 0, 1)$ direction. We remove the periodic boundary conditions such that the ends are closed and each antiskyrmion interacts with only one other. We then seed two antiskyrmions by defining circular regions of diameter $L/8$ with $\mathbf{m} = (0, 0, -1)$ at a distance of $\pm\kappa L$ along the x -axis from the centre, where κ is some variable dimensionless ratio which we aim to measure the total energy of the system (and hence the stability) as a function of. The timescale of the simulation should be greater than the short-timescale dynamics of the formation of the antiskyrmions, but less than the long-timescale dynamics of the antiskyrmion interactions, for which they move relative to each other. In order to determine the time for which we should run the simulation, we seed a single antiskyrmion using the usual method at the centre of the racetrack and run the simulation for 1 ns. We then plot the average absolute deviation of all of the components of all spins in the system against simulation time. We find that the resulting curve drops rapidly and becomes virtually horizontal at a time of around 0.4 ns, so we take a relaxation time of 0.5 ns in order to counteract any effects on this curve as a result of the inter-antiskyrmion interactions.

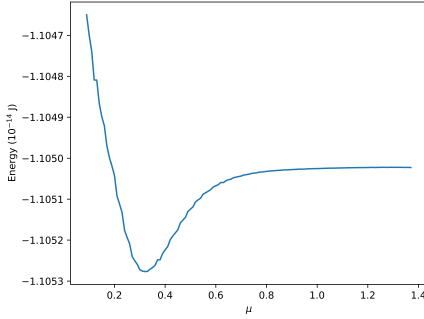


FIG. 23: The total energy of a system of two antiskyrmions in a nanotrack as a function of their separation.

As shown in Fig. 23, the system is the most stable when $\kappa = 0.32$, such that the antiskyrmions are separated by a distance of $0.64L$, demonstrating that the antiskyrmion is attractive at short-range and repulsive at longer ranges.

7.3. Oscillations of Antiskyrmions in a Nanotrack

In order to study the dynamics of antiskyrmions in such a system, we consider seeding the system in a manner similar to that used to produce Fig. 22, but for each antiskyrmion seed region, as we move along the x -axis, we displace it by a distance of μL , alternatively along the $-\hat{x}$ and $+\hat{x}$ directions. As previously, we vary μ in order to determine the equilibrium configuration.

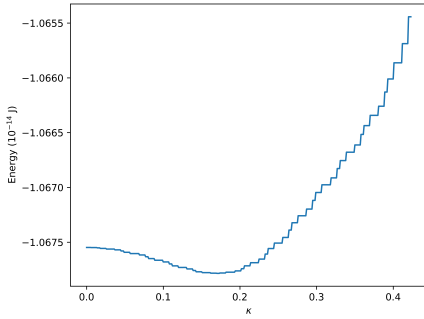


FIG. 24: The total energy of a system of antiskyrmions in a nanotrack similar to that shown in Fig. 22, as a function of the shift of each antiskyrmion from the situation of equal separation.

Fig. 24 shows that we achieve an energy minimum when $\mu = 0.172$, while the case in which the antiskyrmions are equally-spaced when $\mu = 0$ is at an unstable equilibrium. In order to analyse oscillations about this equilibrium position, we relax the system a small distance away from the energy minimum, at $\mu = 0.18$, and relax the system for 0.5 ps in the usual manner. We then decrease α to 0.002, and run the simulation for 50 ns. Calculating the spatially-resolved power spectral density of this system gives a single peak at 0.17 GHz, which is the frequency



FIG. 25: The oscillation of antiskyrmions displaced from their position of minimal energy in a magnetic nanotrack.

of the resulting oscillations about the equilibrium positions of the antiskyrmions. We show the resulting motion for a simulation with $\mu = 0.24$ (which has the same qualitative behaviour) in Fig. 25, as the small amplitude at $\mu = 0.18$ means the oscillations are difficult to see in a sequence of still images. At a close range, the antiskyrmions repel each other, exerting a force with a component along both the x - and y -axes, resulting in the antiskyrmions moving in an ellipse.

8. CONCLUSIONS AND FURTHER WORK

8.1. Conclusions

Using micromagnetic simulations, we have demonstrated the existence of a wealth of excitation modes of antiskyrmions in confined geometries, which has implications for the prediction of their behaviour in devices which rely on their confinement. We have also shown that similar dynamics occur in quasi-infinite geometries for which antiskyrmions arrange themselves into lattices, the typical situation for which skyrmions and antiskyrmions are observed experimentally. Additionally, we have shown that the interaction between antiskyrmions is attractive at long-range and repulsive at shorter length scales, which disfavours the equal spacing of 1D antiskyrmion lattices, such as those which would be found in proposed racetrack memory devices. Furthermore, we have demonstrated that the formation of antiskyrmions away from their equilibrium positions in such a device results in oscillations with frequencies several orders of magnitude lower than those of their internal dynamics.

8.2. Potential Future Investigations

Natural extensions to this project would be to compare the resonance frequencies obtained using the ringdown method and eigenvalue methods with those obtained with other methods such as collective coordinate modelling,^{69,70} which could be applied to better understand the emergent dynamics of such excitation modes. Another potential course of investigation could be to attempt to simulate 2D lattice modes, in which antiskyrmions in a lattice move relative to one another. The excitation of such modes may be possible through the application of spatially non-uniform fields to the sample.

Acknowledgments

I would like to thank Prof Peter Hatton for his initial ideas for the project and support throughout. For their sustained suggestions and help with micromagnetic modelling techniques, I would like to thank the following members of the Computational Modelling Group at the University of Southampton: Dr David Cortés-Ortuño, Mr Ryan Pepper, Ms Vanessa Nehruji, and Dr Marijan Beg, as well as Dr Ondrej Hovorka and Mr Gary Downing for their mathematical expertise and additional input. I would also like to express appreciation to Mr Max Birch for acting as a valuable link between this computational work and experimental work in this area, providing inspiration for the investigations.

References

- ¹ T. H. R. Skyrme and B. F. J. Schonland, Proceedings of the Royal Society of London. Series A. Mathematical and Physical Sciences **247**, 260 (1958).
- ² T. H. R. Skyrme and B. F. J. Schonland, Proceedings of the Royal Society of London. Series A. Mathematical and Physical Sciences **260**, 127 (1961).
- ³ T. H. R. Skyrme and W. G. Penney, Proceedings of the Royal Society of London. Series A. Mathematical and Physical Sciences **262**, 237 (1961).
- ⁴ J. Perring and T. Skyrme, Nuclear Physics **31**, 550 (1962).
- ⁵ T. Skyrme, Nuclear Physics **31**, 556 (1962).
- ⁶ T.-L. Ho, Phys. Rev. Lett. **81**, 742 (1998).
- ⁷ A. Knigavko and B. Rosenstein, Phys. Rev. Lett. **82**, 1261 (1999).
- ⁸ J.-i. Fukuda and S. Žumer, Nature Communications **2**, 246 EP (2011).
- ⁹ A. N. Bogdanov and D. Yablonskii, Zh. Eksp. Teor. Fiz. **95**, 178 (1989).
- ¹⁰ A. Bogdanov and A. Hubert, Journal of Magnetism and Magnetic Materials **138**, 255 (1994).
- ¹¹ A. Bogdanov, ZhETF Pisma Redaktsiiu **62**, 231 (1995).
- ¹² A. Bogdanov and A. Hubert, Journal of Magnetism and Magnetic Materials **195**, 182 (1999).
- ¹³ A. N. Bogdanov and U. K. Rößler, Phys. Rev. Lett. **87**, 037203 (2001).
- ¹⁴ U. K. Rößler, A. N. Bogdanov, and C. Pfleiderer, Nature **442**, 797 EP (2006).
- ¹⁵ S. Mühlbauer, B. Binz, F. Jonietz, C. Pfleiderer, A. Rosch, A. Neubauer, R. Georgii, and P. Böni, Science **323**, 915 (2009).
- ¹⁶ X. Z. Yu, Y. Onose, N. Kanazawa, J. H. Park, J. H. Han, Y. Matsui, N. Nagaosa, and Y. Tokura, Nature **465**, 901 EP (2010).
- ¹⁷ M. Ezawa, Phys. Rev. Lett. **105**, 197202 (2010).
- ¹⁸ T. Okubo, S. Chung, and H. Kawamura, Phys. Rev. Lett. **108**, 017206 (2012).
- ¹⁹ S. Heinze, K. von Bergmann, M. Menzel, J. Brede, A. Kubetzka, R. Wiesendanger, G. Bihlmayer, and S. Blügel, Nature Physics **7**, 713 EP (2011).
- ²⁰ J. Müller, *Magnetic Skyrmions and Topological Domain Walls*, Ph.D. thesis, Universität zu Köln (2018).
- ²¹ W. Koshiba and N. Nagaosa, New Journal of Physics **18**, 045007 (2016).

- ²² W. Jiang, P. Upadhyaya, W. Zhang, G. Yu, M. B. Jungfleisch, F. Y. Fradin, J. E. Pearson, Y. Tserkovnyak, K. L. Wang, O. Heinonen, S. G. E. te Velthuis, and A. Hoffmann, *Science* **349**, 283 (2015).
- ²³ A. Bernand-Mantel, L. Camosi, A. Wartelle, N. Rougemaille, M. Darques, and L. Ranno, *SciPost Physics* **4** (2017), 10.21468/SciPostPhys.4.5.027.
- ²⁴ A. K. Nayak, V. Kumar, T. Ma, P. Werner, E. Pippel, R. Sahoo, F. Damay, U. K. Rößler, C. Felser, and S. S. P. Parkin, *Nature* **548**, 561 EP (2017).
- ²⁵ J. M. Shalf and R. Leland, *Computer* **48**, 14 (2015).
- ²⁶ S. Krishnan, S. V. Garimella, G. M. Chrysler, and R. V. Mahajan, *IEEE Transactions on Advanced Packaging* **30**, 462 (2007).
- ²⁷ S. E. Thompson and S. Parthasarathy, *Materials Today* **9**, 20 (2006).
- ²⁸ W. Kang, Y. Huang, X. Zhang, Y. Zhou, and W. Zhao, *Proceedings of the IEEE* **104**, 2040 (2016).
- ²⁹ A. Fert, N. Reyren, and V. Cros, *Nature Reviews Materials* **2**, 17031 EP (2017).
- ³⁰ S. S. P. Parkin, M. Hayashi, and L. Thomas, *Science* **320**, 190 (2008).
- ³¹ R. Tomasello, E. Martinez, R. Zivieri, L. Torres, M. Carpentieri, and G. Finocchio, *Scientific Reports* **4**, 6784 EP (2014).
- ³² X. Zhang, G. P. Zhao, H. Fangohr, J. P. Liu, W. X. Xia, J. Xia, and F. J. Morvan, *Scientific Reports* **5**, 7643 EP (2015).
- ³³ S. Woo, K. M. Song, X. Zhang, Y. Zhou, M. Ezawa, X. Liu, S. Finizio, J. Raabe, N. J. Lee, S.-I. Kim, S.-Y. Park, Y. Kim, J.-Y. Kim, D. Lee, O. Lee, J. W. Choi, B.-C. Min, H. C. Koo, and J. Chang, *Nature Communications* **9**, 959 (2018).
- ³⁴ C. Song, C. Jin, H. Xia, J. Wang, Y. Ma, J. Wang, and Q. Liu, *arXiv preprint arXiv:1810.02464* (2018).
- ³⁵ M. Beg, *Skyrmionic states in confined helimagnetic nanostructures*, Ph.D. thesis, University of Southampton (2016).
- ³⁶ G. S. Abo, Y. Hong, J. Park, J. Lee, W. Lee, and B. Choi, *IEEE Transactions on Magnetics* **49**, 4937 (2013).
- ³⁷ D. Cortes-Ortuno, M. Beg, V. Nehruji, L. Breth, R. Pepper, T. Kluyver, G. Downing, T. Hesjedal, P. Hatton, T. Lancaster, R. Hertel, O. Hovorka, and H. Fangohr, *New Journal of Physics* **20**, 113015 (2018).
- ³⁸ S. Rohart and A. Thiaville, *Phys. Rev. B* **88**, 184422 (2013).
- ³⁹ H. Fangohr, G. Bordignon, M. Franchin, A. Knittel, P. A. J. de Groot, and T. Fischbacher, *Journal of Applied Physics* **105**, 07D529 (2009).
- ⁴⁰ L. D. Landau and E. M. Lifshitz, *Phys. Z. Sowjetunion* **8**, 101 (1935).
- ⁴¹ T. L. Gilbert, *IEEE Transactions on Magnetics* **40**, 3443 (2004).
- ⁴² A. Vansteenkiste, J. Leliaert, M. Dvornik, M. Helsen, F. Garcia-Sanchez, and B. Van Waeyenberge, *AIP Advances* **4**, 107133 (2014).
- ⁴³ M. Mruczkiewicz, P. Gruszecki, M. Krawczyk, and K. Y. Guslienko, *Phys. Rev. B* **97**, 064418 (2018).
- ⁴⁴ U. Ritzmann, S. von Malottki, J.-V. Kim, S. Heinze, J. Sinova, and B. Dupé, *Nature Electronics* **1**, 451 (2018).
- ⁴⁵ M. Hoffmann, B. Zimmermann, G. P. Müller, D. Schürhoff, N. S. Kiselev, C. Melcher, and S. Blügel, *Nature Communications* **8**, 308 (2017).
- ⁴⁶ W. Heisenberg, *Zeitschrift für Physik* **38**, 411 (1926).
- ⁴⁷ H. Kronmüller and S. Parkin, *Handbook of Magnetism and Advanced Magnetic Materials*, Vol. 2 (Wiley, 2007) p. 753.
- ⁴⁸ I. Dzyaloshinsky, *Journal of Physics and Chemistry of Solids* **4**, 241 (1958).
- ⁴⁹ T. Moriya, *Phys. Rev.* **120**, 91 (1960).
- ⁵⁰ L. Camosi, S. Rohart, O. Fruchart, S. Pizzini, M. Belmeguenai, Y. Roussigné, A. Stashkevich, S. M. Cherif, L. Ranno, M. de Santis, and J. Vogel, *Phys. Rev. B* **95**, 214422 (2017).
- ⁵¹ M. Albert, *Domain wall dynamics and resonant modes of magnetic nanostructures*, Ph.D. thesis, University of Southampton (2016).
- ⁵² R. Yanes, O. Chubykalo-Fesenko, H. Kachkachi, D. A. Garanin, R. Evans, and R. W. Chantrell, *Phys. Rev. B* **76**, 064416 (2007).
- ⁵³ M. Beg, M. Albert, M.-A. Bisotti, D. Cortes-Ortuno, W. Wang, R. Carey, M. Vouzden, O. Hovorka, C. Ciccarelli, C. S. Spencer, C. H. Marrows, and H. Fangohr, *Physical Review B* **95**, 1 (2017).
- ⁵⁴ B. Krüger, *Current-Driven Magnetization Dynamics: Analytical Modeling and Numerical Simulation*, Ph.D. thesis, Universität Hamburg (2011).
- ⁵⁵ C. Abert, L. Exl, G. Selke, A. Drews, and T. Schrefl, *Journal of Magnetism and Magnetic Materials* **326**, 176 (2013).
- ⁵⁶ A. Baker, M. Beg, G. Ashton, M. Albert, D. Chernyshenko, W. Wang, S. Zhang, M.-A. Bisotti, M. Franchin, C. L. Hu, R. Stamps, T. Hesjedal, and H. Fangohr, *Journal of Magnetism and Magnetic Materials* **421**, 428 (2017).
- ⁵⁷ M. d'Aquino, C. Serpico, G. Miano, and C. Forestiere, *Journal of Computational Physics* **228**, 6130 (2009).
- ⁵⁸ M. Beg, R. Carey, W. Wang, D. Cortés-Ortuno, M. Vouzden, M.-A. Bisotti, M. Albert, D. Chernyshenko, O. Hovorka, R. L. Stamps, and H. Fangohr, *Scientific Reports* **5**, 17137 EP (2015).
- ⁵⁹ S. Sen, C. Singh, P. K. Mukharjee, R. Nath, and A. K. Nayak, *Phys. Rev. B* **99**, 134404 (2019).
- ⁶⁰ A. Aranda, A. Hierro-Rodriguez, G. Kakazei, O. Chubykalo-Fesenko, and K. Guslienko, *Journal of Magnetism and Magnetic Materials* **465**, 471 (2018).
- ⁶¹ A. Antoniou, *Digital Signal Processing: Signals, Systems, and Filters* (McGraw-Hill Professional, 2005).
- ⁶² J. Waizner, *Spin wave excitations in magnetic helices and skyrmion lattices*, Ph.D. thesis, Universität zu Köln (2016).
- ⁶³ Z. V. Gareeva and K. Y. Guslienko, *Journal of Physics Communications* **2**, 035009 (2018).
- ⁶⁴ L. Camosi, N. Rougemaille, O. Fruchart, J. Vogel, and S. Rohart, *Phys. Rev. B* **97**, 134404 (2018).
- ⁶⁵ M. Leroux, M. J. Stolt, S. Jin, D. V. Pete, C. Reichhardt, and B. Maiorov, *Scientific Reports* **8**, 15510 (2018).
- ⁶⁶ K. Shibata, A. Kovács, N. S. Kiselev, N. Kanazawa, R. E. Dunin-Borkowski, and Y. Tokura, *Phys. Rev. Lett.* **118**, 087202 (2017).
- ⁶⁷ S.-Z. Lin, C. Reichhardt, C. D. Batista, and A. Saxena, *Phys. Rev. B* **87**, 214419 (2013).
- ⁶⁸ H. Du, X. Zhao, F. N. Rybakov, A. B. Borisov, S. Wang, J. Tang, C. Jin, C. Wang, W. Wei, N. S. Kiselev, Y. Zhang, R. Che, S. Blügel, and M. Tian, *Phys. Rev. Lett.* **120**, 197203 (2018).
- ⁶⁹ B. F. McKeever, D. R. Rodrigues, D. Pinna, A. Abanov, J. Sinova, and K. Everschor-Sitte, *Phys. Rev. B* **99**, 054430 (2019).
- ⁷⁰ D. J. Clarke, O. A. Tretiakov, G.-W. Chern, Y. B. Bazaliy, and O. Tchernyshyov, *Phys. Rev. B* **78**, 134412 (2008).

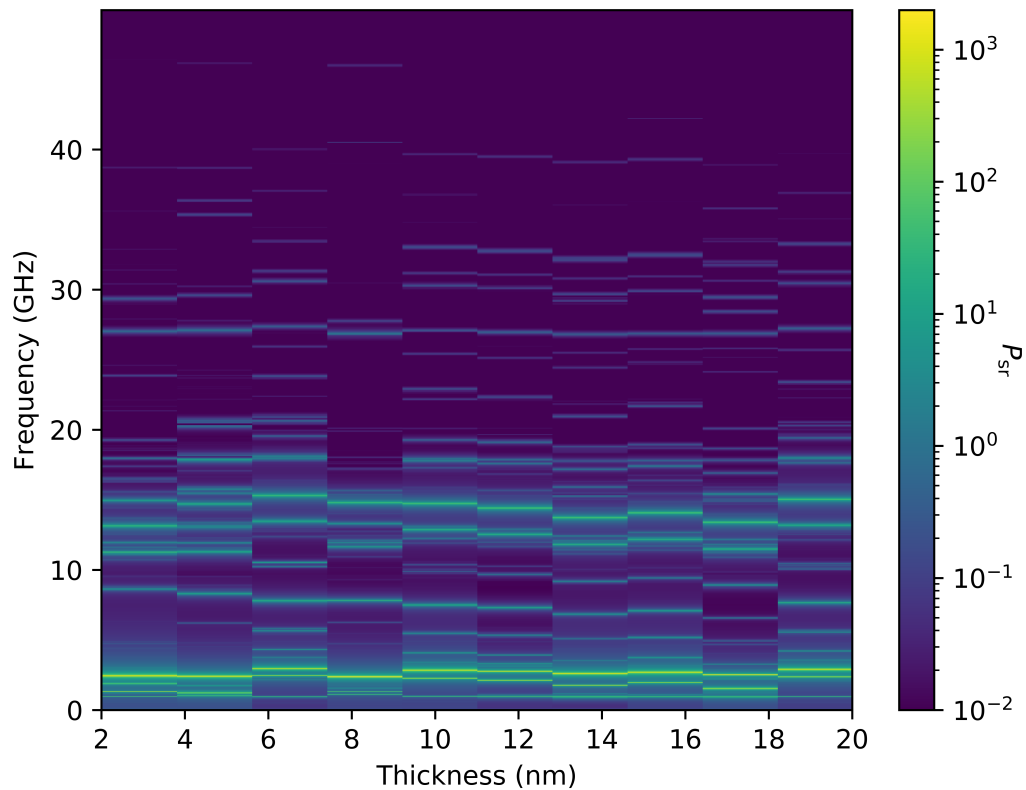
Appendix A: Effect of Sample Thickness on the Power Spectra

FIG. A1: Variation of the spatially-resolved power spectral density for in-plane excitations of an antiskyrmion in a nanodisk with the thickness of the nanodisk.

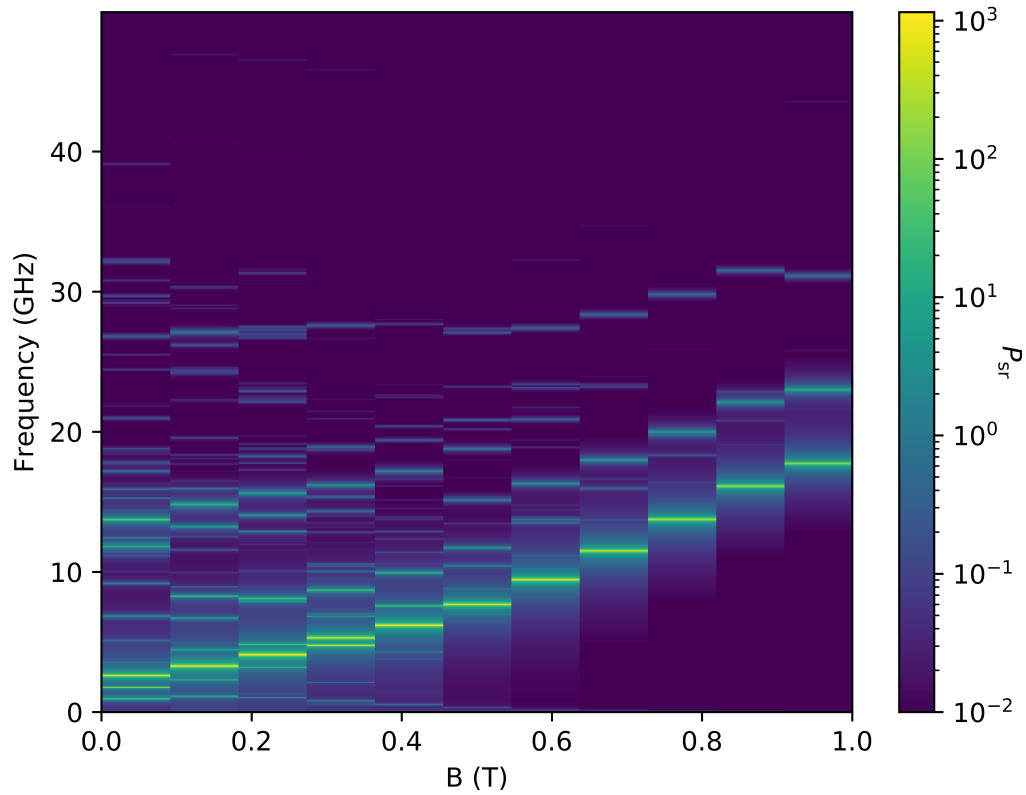
Appendix B: Effect of Externally-Applied Field on the Power Spectra


FIG. A2: Variation of the spatially-resolved power spectral density for in-plane excitations of an antiskyrmion in a nanodisk with the externally-applied magnetic field along z .